Proceedings of the
Annual Stability Conference
Structural Stability Research Council
St. Louis, Missouri April 2-5, 2019

Spherically-hinged cold-formed steel equal-leg angle columns: experimental investigation and DSM design

Kathleen Guimarães Santana[1], Alexandre Landesmann[1], Dinar Camotim[2] and Pedro Borges Dinis[2]

Abstract

Recently, Dinis & Camotim (2017) performed an in-depth numerical investigation aimed at developing, validating and assessing the merits of a novel Direct Strength Method design approach for short-to-intermediate cold-formed steel simply supported equal-leg angle columns – the end cross-sections are prevented from warping and torsion, and pinned with respect to major and minor-axis bending, which amounts to being rigidly attached to rigid plates resting on spherical hinges ("spherically-hinged columns"). However, a shortcoming of the above investigation was the lack of experimental validation, due to the fact that no available experimental failures loads concerning these columns were found in the literature. The research work reported in this paper provides a contribution towards filling this gap, since it consists of an experimental study, carried out at COPPE (Federal University of Rio de Janeiro), on the behavior and load-carrying capacity of cold-formed steel spherically-hinged equal-leg angle columns. After addressing the selection of the columns to be tested, the experimental set-up and test procedure are described in detail and the results obtained are presented and discussed. Such results comprise (i) initial geometrical imperfection measurements, (ii) equilibrium paths relating the applied load to key column displacements, (iii) deformed configurations (including the collapse modes) and (iv) failure loads. Next, attention is turned to assessing the merits of the DSM-based design approach proposed by Dinis & Camotim (2017). The comparison between the (i) experimental failure loads obtained in this work, as well as the previously available numerical ones, with (ii) their estimates provided by the novel DSM-based strength curves shows a very good correlation – thus, it may be rightfully argued that the validation and calibration of this design approach has been successfully achieved.

1. Introduction

Equal-leg angle members have been traditionally used in structural engineering applications, such as (i) bracing rods for buildings, (ii) components of built-up columns, trusses and lattice girders, or (iii) the routine construction of transmission towers construction. However, despite their geometrical simplicity, angle members, namely columns, exhibit a rather complex structural behavior, which has been defying researchers and engineers for quite a long time.

Although the non-linear behavior, strength and design of short-to-intermediate angle columns has attracted a lot of attention for several decades (*e.g.*, Kitipornchai & Chan 1987, Kitipornchai *et al.* 1990,

[1] Civil Engineering Program, COPPE, Universidade Federal do Rio de Janeiro. <kathleen; alandes@coc.ufrj.br>
[2] CERIS, DECivil, Instituto Superior Técnico, Universidade de Lisboa. <dcamotim; dinis@civil.ist.utl.pt>

Popovic *et al.* 1999, Young 2004, Ellobody & Young 2005, Rasmussen 2005, 2006, Chodraui *et al.* 2006, Maia *et al.* 2008, Shifferaw & Schafer 2011 and Mesacasa Jr. 2012), it was not until the last few years that the mechanics underlying this non-linear behavior were unveiled and properly understood (*e.g.*, Dinis *et al*. 2012, Mesacasa *et al*. 2014), in the context of columns with fixed-ended and cylindrically-hinged support conditions[3]. Dinis *et al.* (2012) unveiled that the non-linear behaviors of such columns are (i) both strongly influenced by the interaction between major-axis flexural-torsional and minor-axis flexural buckling (a quite unique global-global coupling phenomenon) and (ii) markedly different, due to the effective centroid shift effects appearing in the pin-ended (cylindrically-hinged) columns.

The above findings led Dinis & Camotim (2015) to propose a novel, rational and unified design approach applicable to both fixed-ended and cylindrically-hinged (pin-ended) columns, which is based on the Direct Strength Method (DSM – *e.g.*, Schafer 2008, Camotim *et al.* 2016) and combines (i) numerically-based genuine flexural-torsional (FT) strength curves, specifically developed for this purpose, with (ii) the currently codified DSM global design curve. This design approach was shown to be both accurate and reliable – indeed, the prediction quality of the available experimental and numerical failure loads allows for the use of an LRFD resistance factor equal ϕ_c=0.85, value recommended for all other compression members by the current North American Specification (AISI 2016). The above design approach was subsequently slightly improved by Landesmann *et al.* (2016) and, finally cast in a simpler form, better suited for codification, by Dinis & Camotim (2018). Later, these same authors (Dinis & Camotim 2016, Dinis *et al.* 2016) extended the scope of their and reported numerical investigations on the behavior and DSM-based design of hot-rolled steel fixed-ended and cylindrically-hinged (pin-ended) short-to-intermediate equal-leg angle columns, which differ from their cold-formed counterparts in the fact that they (i) exhibit much stockier legs (lower width-to-thickness ratios) and (ii) are visibly affected by residual stress effects. These numerical studies provided fairly solid evidence that the DSM-based design approach developed for cold-formed steel columns can also be applied to hot-rolled ones counterparts – however, the experimental validation of this assertion is still lacking.

Very recently, Dinis & Camotim (2017) addressed the behavior and DSM-based design of fully simply supported short-to-intermediate hot-rolled and cold-formed steel equal-leg angle columns – the end cross-sections are prevented from warping and torsion, and pinned with respect to major and minor-axis bending, which amounts to being rigidly attached to rigid plates that are resting on spherical hinges ("spherically-hinged columns", termed here in abbreviate form as "SH columns"). They gathered the experimental failure loads available in the literature, which were found to exist only for hot-rolled columns, obtained numerical failure loads and used the whole failure load set to develop and validate a DSM-based design approach for the SH columns. Due to change in end support conditions concerning major-axis bending (pinned instead of fixed), with respect to the fixed-ended or cylindrically hinged columns addressed previously, new sets of length-dependent flexural-torsional strength and reduction factor curves and had to be numerically developed. Nevertheless, the concepts and procedures involved are similar to those employed earlier for the fixed-ended and cylindrically hinged columns (*e.g.*, Dinis & Camotim 2015, 2018). This new/modified DSM-based design approach was shown to yield safe and reliable estimates of the short-to-intermediate hot-rolled (experimental and numerical) and cold-formed (numerical) column failure loads. However, in the case of the cold-formed steel columns, no experimental validation was possible, due to the lack of test results. The objective of this work is to contribute towards filling this gap, by presenting an experimental investigation concerning short-to-intermediate SH columns.

[3] End cross-sections prevented from warping and torsion, fixed with respect to major-axis bending and pinned with respect to minor-axis bending.

This work reports an experimental investigation, carried out at COPPE (Federal University of Rio de Janeiro), concerning cold-formed steel short-to-intermediate spherically-hinged equal-leg angle columns. After presenting an overview of the DSM-based design procedure proposed by Dinis & Camotim (2017), the paper addresses the geometry selection of the column specimen to be tested. Next, following a fairly detailed description of the test set-up and procedure employed, the experimental results obtained are presented and discussed in great depth. Such experimental results consist of (i) initial imperfection measurements, (ii) equilibrium paths relating the applied load to key column displacements, (iii) deformed configurations (including the collapse modes) and (iv) failure loads. Then, attention is turned to assessing the merits of the above DSM-based design approach, which is achieved through the comparison of (i) the experimental and numerical failure loads obtained in this work and reported by Dinis & Camotim (2017), respectively, and (ii) the corresponding estimates provided and the proposed strength curves. It is shown that a very good correlation, qualitatively similar to that obtained previously for the fixed-ended and cylindrically-hinged columns, making it possible to argue that the validation and calibration of the proposed design approach may be deemed (successfully) completed – in particular, it should be noted that the LRFD (Load and Resistance Factor Design) resistance factor calculated on the basis of the results presented in this work is higher than ϕ_c=0.85, value recommended for all other compression members by the current North American Specification (AISI 2016), thus paving the way to the future codification of the proposed design approach. Finally, the paper closes with a few concluding remarks.

2. Overview of the DSM-Based Design Approach for SH Angle Columns

As mentioned above, Dinis & Camotim (2017) recently developed a DSM-based design approach for SH cold-formed steel short-to-intermediate equal-leg angle columns, based on the same concepts employed to propose the nearly codified methodology for their fixed-ended and cylindrically-hinged counterparts (Dinis & Camotim 2018). The main features of this design approach are the following:

(i) It is based on the fact that short-to-intermediate angle columns fail in interactive modes combing major-axis flexural-torsional and minor-axis flexural deformations.

(ii) It involves the use of (ii_1) the currently codified DSM global design curve and (ii_2) a set of genuine FT strength curves, developed for columns with minor-axis bending fully prevented.

(iii) The above flexural-torsional curves make it possible to capture the progressive decrease of the column post-critical strength as its length increases (within the $P_{cr}(L)$ curve plateau).

(iv) The effective centroid shift effects, strongly affecting the failure loads of the columns pinned with respect to the minor-axis bending, are included in the design approach via a parameter β, which also reflects the length-dependence of the column FT behavior (within the $P_{cr}(L)$ curve plateau).

(v) The length dependence of the column FT post-critical strength and effective centroid shift effects is quantified by means of a parameter Δ_f, defined by

$$\Delta_f = \frac{f_{bt} - f_{crft}}{f_{bt}} \times 100 \quad , \tag{1}$$

where f_{bt} and f_{crft} are the pure torsional and major-axis flexural-torsional (critical) buckling stresses, which can be determined exactly by means of the analytical expressions

$$f_{bt} = G\frac{t^2}{b^2} + \pi^2 \frac{E \cdot t^2}{12\left(L/2\right)^2} \tag{2}$$

$$f_{bf} = \frac{\pi^2 E\ b^2}{6\ L^2} \tag{3}$$

$$f_{crft} = \frac{4}{5}\left(f_{bt} + f_{bf} - \sqrt{\left(f_{bt} + f_{bf} \right)^2 - 2.5\, f_{bt}\, f_{bf}} \right) \quad , \tag{4}$$

where b, t and L are the column leg width, thickness and length, and E is the material (steel) Young's modulus – note that f_{bf} is the column pure major-axis flexural buckling stress (needed to calculate f_{crft}).

The angle column nominal strength against the interactive failures under consideration (f_{nfte}) is given by[4]

$$f_{nfte} = \begin{cases} \beta \cdot f_{ne} & \text{if} \quad \lambda_{fte} \le \left(0.5 + \sqrt{0.25 - b}\right)^{\frac{1}{2a}} \\ \beta \cdot f_{ne} \left(\dfrac{f_{crft}}{f_{ne}} \right)^a \left[1 - b \left(\dfrac{f_{crft}}{f_{ne}} \right)^a \right] & \text{if} \quad \lambda_{fte} > \left(0.5 + \sqrt{0.25 - b}\right)^{\frac{1}{2a}} \end{cases} \quad \text{with } \lambda_{fte} = \sqrt{\frac{f_{ne}}{f_{crft}}} \quad , \tag{5}$$

where the reduction parameter β and the minor-axis flexural strength f_{ne} are given by the expressions

$$\beta = \frac{0.68}{\left(\lambda_{fte} - c\right)^d} \le 1 \tag{6}$$

$$f_{ne} = \begin{cases} f_y \left(0.658^{\lambda_c^2} \right) & \text{if} \quad \lambda_c \le 1.5 \\ f_y \left(\dfrac{0.877}{\lambda_c^2} \right) & \text{if} \quad \lambda_c > 1.5 \end{cases} \quad \text{with} \quad \lambda_c = \sqrt{\frac{f_y}{f_{cre}}} \text{ and } f_{cre} = \frac{\pi^2 E\ b^2}{24\ L^2} \quad . \tag{7}$$

Note that, in equation (5), the slenderness λ_{fte} is based on the column nominal strength against minor-axis flexural collapse (f_{ne}), which is obtained from the codified DSM global design curve given by equation (7) – f_{cre} is the column minor-axis flexural buckling stress and f_y is the material (steel) yield stress. The length dependence of the column nominal strength against interactive failures (f_{nfte}), stemming from the combined influence of the FT post-critical strength and effective centroid shift effects, is captured by means of the parameters a, b, c and d appearing in equations (5) (a and b) and (6) (c and d) – these parameters depend on the percentage ratio Δ_f through the expressions

$$a = \begin{cases} -0.001\ \Delta_f^3 + 0.014\ \Delta_f^2 - 0.007\ \Delta_f + 0.4 & \text{if} \quad \Delta_f \le 1 \\ 0.001\ \Delta_f^2 + 0.04\ \Delta_f + 0.365 & \text{if} \quad 1 < \Delta_f < 10 \\ 0.865 & \text{if} \quad \Delta_f \ge 10 \end{cases} \tag{8}$$

$$b = \begin{cases} -0.001\ \Delta_f^3 + 0.001\ \Delta_f^2 - 0.011\ \Delta_f + 0.15 & \text{if} \quad \Delta_f \le 1 \\ 0.005\ \Delta_f + 0.134 & \text{if} \quad 1 < \Delta_f < 10 \\ 0.184 & \text{if} \quad \Delta_f \ge 10 \end{cases} \tag{9}$$

[4] Note that the letter "b" in Eq. (5) should not be confused with the angle leg width.

$$c = \begin{cases} -300\ \Delta_f^3 + 110\ \Delta_f^2 - 12.8\ \Delta_f + 1 & \text{if} \quad \Delta_f \le 0.2 \\ -0.001\ \Delta_f^3 + 0.01\ \Delta_f^2 - 0.058\ \Delta_f + 0.451 & \text{if} \quad 0.2 < \Delta_f < 8 \\ 0.115 & \text{if} \quad \Delta_f \ge 8 \end{cases} \tag{10}$$

$$d = \begin{cases} 290\ \Delta_f^3 - 98\ \Delta_f^2 + 10.8\ \Delta_f + 0.25 & \text{if} \quad \Delta_f \le 0.2 \\ -0.001\ \Delta_f^2 + 0.03\ \Delta_f + 0.804 & \text{if} \quad 0.2 < \Delta_f < 9.5 \\ 0.999 & \text{if} \quad \Delta_f \ge 9.5 \end{cases} . \tag{11}$$

Finally, the column failure loads are given by

$$P_n = A \cdot f_{nfte} \quad . \tag{12}$$

3. Selection of the Column Specimen Geometries – Buckling Analysis

The first stage of this work consisted of careful selecting the cross-section dimensions and lengths of the SH column specimens to be tested experimentally – recall that these columns (i) are pinned with respect to minor and major-axis flexure, and (ii) have fully prevented torsional rotations and (secondary) warping. The selection procedure involved sequences of buckling (linear stability) analyses, performed using the code GBTUL, based on Generalized Beam Theory (GBT) (Bebiano *et al.* 2018). The aim was to identify equal-leg angle columns (i) with cross-section dimensions commonly used in practice, (ii) buckling in flexural-torsional modes (*i.e.*, with short-to-intermediate lengths), and (ii) exhibiting a fairly wide slenderness range ($\sim 1 \le \lambda_{fte} \le \sim 3.5$). In addition, it was necessary to comply with the test set-up and specimen fabrication restraints, namely (i) specimens no longer than *1200 mm* and (ii) structural sheets with nominal thickness equal to *t=0.80, 0.95* or *1.25 mm* and made of mild steel with nominal Young's modulus, Poisson's ratio and yield stress equal to $E = 205\ GPa$, $\nu = 0.3$ and $f_y \approx 366\ MPa$, respectively.

Fortunately, it was possible to fulfill the requirements listed in the previous paragraph and the selection procedure led to the angle column geometries given in Table 1 – *2* leg widths (*b=25* and *50 mm*), 3 nominal thickness value (*t=0.80, 0.95* and *1.25 mm*) and various lengths. These column geometries are divided in four groups, each concerning a given cross-section dimension set (*i.e.*, leg width and thickness) – the column specimen label provides the cross-section (C1 to C4) and length (in *mm*) – *e.g.*, column C1-400 has cross-section C1 (*b=25 mm* and *t=0.80 mm*) and length equal to *400 mm*. Table 1 also provides the column (i) areas *A*, (ii) squash loads $P_y = A \cdot f_y$ (for $f_y = 366\ MPa$), (iii) flexural-torsional (critical – $P_{cr.ft}$) and torsional (P_{bt}) buckling loads, (iv) Δ_f ratios (see Eq. (1)), (v) global failure load estimates f_{ne} and (vi) slenderness values λ_{fte} – note that one has $0.99 \le \lambda_{fte} \le 3.78$. For illustrative purposes, Figs. 1(a)-(b) (i) show the P_{cr} *vs.* L (L in logarithmic scale) curves concerning the four cross-sections considered (C1 to C4) and, on each of them, indicates the lengths of the column specimens selected. The close observation of the values given in Table 1 and the buckling results displayed in Figs. 1(a)-(b) prompts the following remarks:

(i) As expected (Dinis *et al.* 2010), each P_{cr} vs. L curve consists of an initial more or less horizontal plateau, associated with major-axis flexural-torsional buckling, followed by a fast descending branch, associated with minor-axis buckling.

Table 1: Column specimens to be tested: geometry, squash load, buckling loads, Δ_f, f_{ne} and λ_{fte} (f_y=366 *MPa*).

Column label	b (*mm*)	t (*mm*)	L (*mm*)	A (*cm²*)	P_y (*kN*)	P_{crft} (*kN*)	P_{bt} (*kN*)	Δ_f (*%*)	f_{ne} (*MPa*)	λ_{fte}
C1-400	25	0.8	400	0.4	14.64	3.26	3.34	2.41	229.85	1.68
C1-600			600			3.10	3.28	5.41	128.36	1.29
C1-800			800			2.94	3.26	9.73	72.20	0.99
C2-400	50	0.8	400	0.8	29.28	1.83	1.83	0.16	325.82	3.78
C2-600			600			1.70	1.71	0.34	281.73	3.64
C2-800			800			1.66	1.67	0.60	229.85	3.33
C3-400	50	0.95	400	0.95	34.77	3.06	3.07	0.23	325.82	3.18
C3-600			600			2.85	2.86	0.48	281.73	3.06
C3-800			800			2.77	2.79	0.84	229.85	2.81
C3-1000			1000			2.73	2.76	1.30	176.93	2.48
C4-400	50	1.25	400	1.25	45.75	6.96	6.98	0.40	325.82	2.42
C4-600			600			6.47	6.53	0.84	281.73	2.33
C4-800			800			6.27	6.37	1.46	229.85	2.14
C4-1000			1000			6.15	6.29	2.27	176.93	1.90

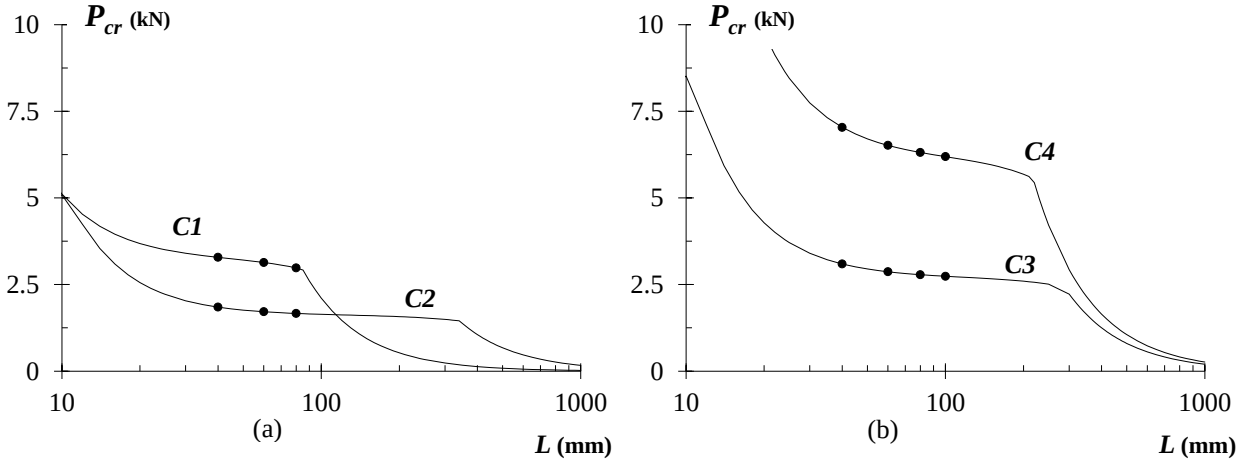

Figure 1: Curves P_{cr} *vs.* L concerning the (a) C1 and C2, and (a) C3 and C4 column cross-section geometries, with the selected specimen lengths indicated on them.

(ii) The column length corresponding to the transition from flexural-torsional buckling to flexural buckling increases with the leg width-to-thickness ratio (b/t). Indeed, for the column cross-sections C2-C3-C4-C1 (*b/t=62.5-52.6-40-31.25*) the above transition occurs for *L=3500-3000-2200-850 mm.*

(iii) For each cross-section dimensions, the value Δ_f grows monotonically with the column length.

(iv) The λ_{fte} values are comprised between *0.99* and *3.78*, thus covering a fairly wide slenderness range. Note that, in general, high λ_{fte} values correspond to short columns – conversely, the longest columns selected (*L=800 or 1000 mm*) exhibit the lowest slenderness values. In order to grasp this apparently surprising feature, look at the λ_{fte} definition, given in Eq. (5): square root of the ratio between the global strength f_{ne} (decreasing very fast with the column length) and the flexural-

torsional (critical) buckling stress f_{crft} (exhibiting a much less pronounced decrease with L, except for very short lengths). Figs. 2(a)-(b), concerning the C2 columns, illustrate the above assertion by showing the variations with L of (iv$_1$) f_{ne} and f_{crft}, and (iv$_2$) λ_{fte} – the length range depicted contains all the values selected. Note that the highest slenderness occurs for $L \approx 400\,mm$, due to the fact that (iv$_1$) f_{ne} decreases continuously with L, (iv$_2$) the f_{crft} vs. L curve displays a maximum at $L < 100\,mm$, followed by a very sharp drop, up to $L \approx 150\,mm$ (from over $400\,MPa$ to about $20\,MPa$), and an almost horizontal plateau for longer columns. Thus, the highest f_{ne}/f_{crft} ratios occur for fairly short columns.

(v) In order to assess the impact of the yield stress on λ_{fte}, Figs. 3(a)-(b) show, for the C2-600 column, the variations with f_y of (v$_1$) f_{ne} and f_{crft}, and (v$_2$) λ_{fte}. Note that increasing the yield stress only leads to a visible slenderness rise up to a certain value (*e.g.*, it is not possible to reach $\lambda_{fte}=5.0$).

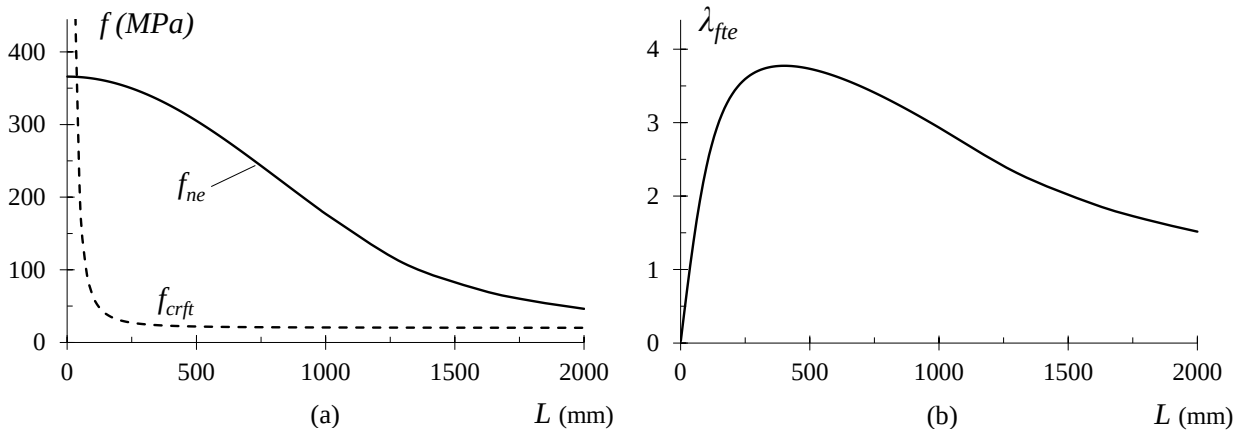

Figure 2: Variation with the length ($0 \le L \le 2000\,mm$) of (a) f_{ne} and f_{crft}, and (b) λ_{fte} for the C2 columns.

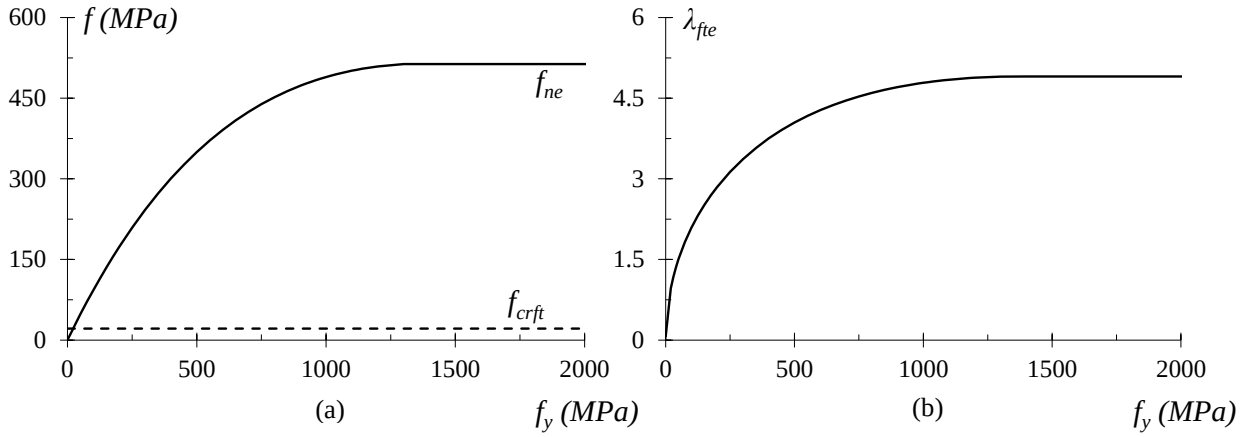

Figure 3: Variation with the yield stress ($f_y \le 2000\,MPa$) of (b) f_{ne} and f_{crft}, and (b) λ_{fte} for the C2-600 column.

4. Experimental Investigation

This section provides a reasonably detailed account of the experimental investigation recently carried out at COPPE (Federal University of Rio de Janeiro) – further details can be found in the work of Santana (2018). After characterizing the column specimens, descriptions of the test set-up and procedure are provided. Then, attention is devoted to presenting and discussing the experimental results recorded and observed prior to and during the tests, namely the specimen initial geometrical imperfections, measured displacements (caused by the applied loading), equilibrium paths, failure loads and collapse mechanisms.

4.1 Column Specimens

The column specimens (i) were manufactured by press braking from zinc-coated structural sheets with nominal thickness values *t=0.8, 0.95* or *1.25 mm* and made of ZAR-345 mild steel, (ii) exhibit the four cross-section geometries given in Table 1 (nominal leg widths equal to *25* or *50 mm*) and (iii) had lengths ranging from *400* to *1000 mm*. Both end cross-sections were fully embedded/cast into *15 mm* thick epoxy-resin plates, which ensure full contact with the test set-up bearing plates while eliminating the need for welding, thus precluding potential residual stress effects and strength reduction at the heat affected zone. Table 3 provides the average values of the measured specimen thickness values, leg widths and lengths – also shown are the locations of the cross-section centroids (G) and principal axes (*1*-major and *2*-minor). The specimen labeling is the same adopted in Table 1 and "R" identifies a repeated specimen (tested to assess the reliability of the experimental set-up and procedure). The cross-section dimensions were measured at five equally spaced locations along the measured specimen length L_0 (0.00-0.25-0.50-0.75-1.00L_0) and the values obtained were found to correlate very well with the nominal ones. Indeed, the ratios between the measured and nominal thickness values, leg widths and lengths varied from *0.98* to *1.01*, *0.982* to *1.04* and *0.998* to *1.003*, respectively. The angles formed by the two legs (θ_b) were also measured at the above five specimen cross-sections and their average and standard deviation values are equal to *87.79*° and *1.38º*, respectively. Finally, note that a press braking manufacturing condition imposed internal bending radii (r_i) approximately equal to the sheet thickness values.

Table 2: Average values of the measured column specimen cross-section dimensions, leg angles, lengths and areas.

Column	b (mm)	t (mm)	θ_b (deg)	L_0 (mm)	A (cm²)
C1-400	25.63	0.80	88	401.3	0.41
C1-400R	25.50	0.80	87	400.5	0.41
C1-600	26.03	0.81	89	601	0.42
C1-800	25.56	0.80	89	800	0.41
C2-400	50.02	0.80	91	401	0.80
C2-400R	49.09	0.80	90	400.5	0.79
C2-600	50.98	0.80	90	600	0.82
C2-600R	52.005	0.80	87	600	0.83
C2-800	50.21	0.80	87	800	0.80
C3-400	49.86	0.96	88	400	0.96
C3-600	50.65	0.96	84	599	0.97
C3-600R	50.65	0.96	86	600	0.97
C3-800	49.86	0.96	88.5	800.8	0.96
C3-1000	49.85	0.96	89.5	1001	0.96
C4-400	50.10	1.23	87	400	1.23
C4-600	50.97	1.22	86	600	1.24
C4-600R	51.13	1.22	86	600	1.25
C4-800	49.85	1.22	87	800.3	1.22
C4-1000	50.01	1.23	88	1001.2	1.23

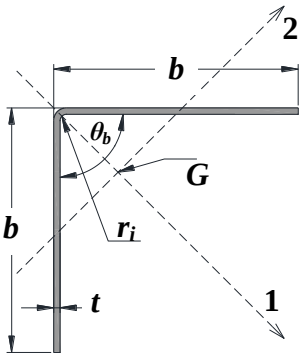

4.2 Mechanical Properties of the Mild Steel

The mechanical properties of the structural ZAR-345 steel (ASTM A653 – ASTM 2011) sheet employed to manufacture the column specimens were experimentally obtained by means of four standard tensile

coupon tests. The coupons were extracted, longitudinally, from virgin steel sheets (belonging to the same batch of those used to manufacture the specimens) prior to the initiation of the cold-forming (press-braking) procedure. The coupon dimensions conformed to ASTM E8/E8M-15a (ASTM 2015) for the tensile testing of metals: *12.5 mm* wide coupons with *50 mm* gauge length ("sheet-type"). Figs. 4(a)-(b) provide a general view of a coupon tensile test and illustrate the type of experimental stress-strain-curves obtained. The tests were performed, as prescribed in ASTM E8/E8M-15a (ASTM 2015), in a Shimadzu AGX-100kN displacement controlled universal testing machine (UTM) and using friction grips. The longitudinal strains were measured through a *50 mm* clip-on gage and two electrical strain gages, attached to each coupon face center (see Fig. 4(a)). A data acquisition system was used to record the load and strain readings at regular intervals during the tests (*15 Hz*). On the basis of the stress-strain curves determined experimentally, it was possible to obtain estimates of the steel mechanical properties – their average values are f_y*=366 MPa* (yield stress), f_u*=458 MPa* (ultimate stress) and *E=205 GPa* (Young's modulus). Moreover, a Poisson's ratio equal to ν*=0.3* was always assumed.

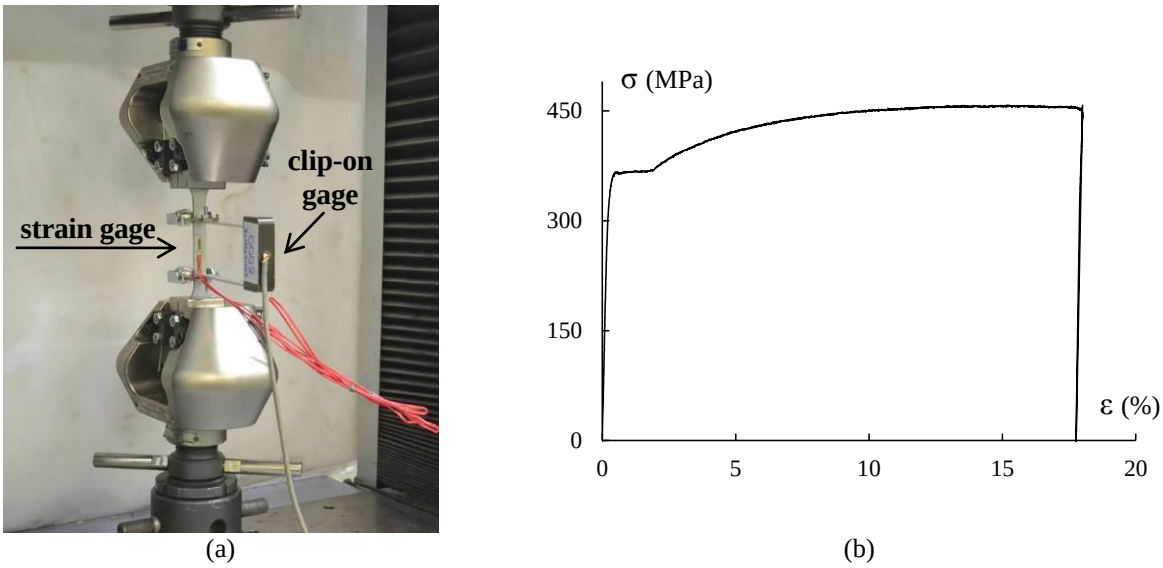

(a) (b)

Figure 4: (a) General view of a coupon tensile test and (b) illustrative stress-strain curve obtained experimentally.

4.3 Test Set-Up

All specimens were tested in a servo-controlled hydraulic steel-frame set-up under displacement-control conditions. The hydraulic jack can supply compressive loads up to *50 kN* and the loads imposed during the performance of a test were measured with a *50 N* accuracy and recorded in a data acquisition system. Figs. 5(a)-(b) provide an overall view and a schematic representation of the test set-up, respectively, showing the (i) moveable frame support, allowing for the testing of specimens with various lengths, (ii) MTS servo-controlled hydraulic jack, (iii) load cell, (iv) column specimen and (v) spherically-hinged support. As for Figs. 6(a)-(b), they provide a general view of the bottom (spherical) end support, which is (i) built from machine-finished carbon steel and (ii) mounted on a *12 mm* thick steel bearing plate – the top end support is similar. These end supports prevent (i) transverse displacements, (ii) torsional rotations, and (iii) local displacements/rotations plus (secondary) warping (recall that specimen end cross-sections are fully embedded into 15 mm thick epoxy-resin plates) – the ensuing support conditions are "pinned" with respect to major and minor axes flexure and, and "fixed" with respect to torsion.

The connection between the specimen end cross-sections (embedded into the epoxy-resin plates) and the spherically-hinged support is preceded by a very careful positioning procedure, aimed at ensuring that

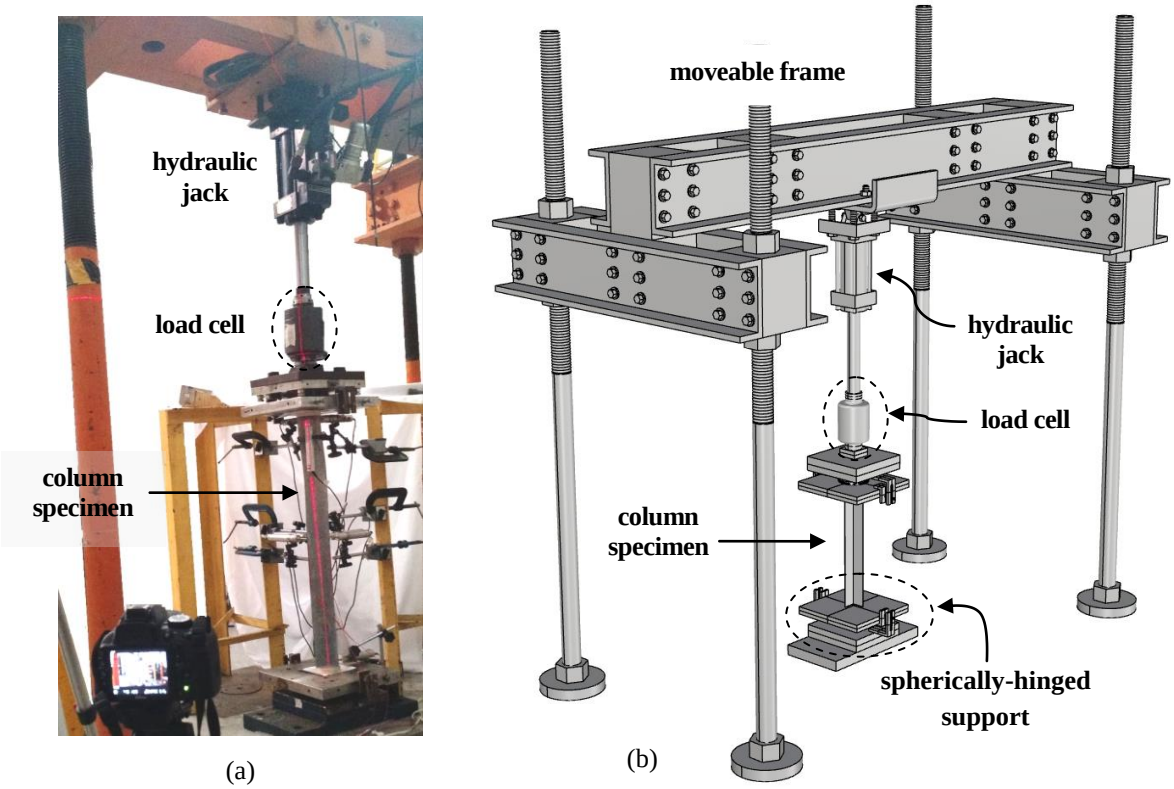

(a) (b)

Figure 5: Experimental steel frame set-up: (a) overall view and (b) 3D schematic representation.

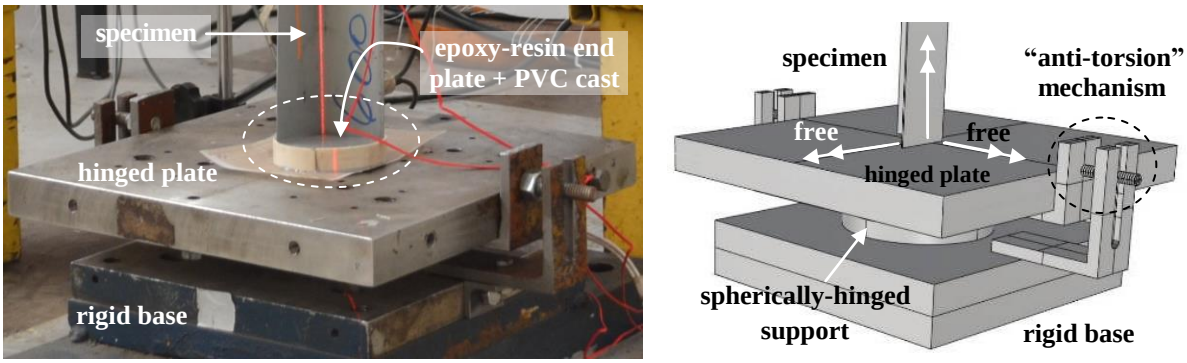

(a) (b)

Figure 6: Specimen bottom spherically-hinged end support: (a) overall view and (b) 3D schematic representation.

the load eccentricities (lack of coincidence between the end cross-section centroids and the test frame loading axis) are minute/negligible. Such procedure involves the following steps:

(i) The actual dimensions of the specimen end cross-sections are carefully measured, in order to enable an accurate definition of the real positions of their centroids.

(ii) Each end cross-section shape and centroid location are marked on "*1 mm* square grid graph paper", so that the cross-section and plate centroids are "perfectly aligned longitudinally" (see Fig. 7(a)).

(iii) After making sure that the centroids are coincident and the end plates are orthogonal to the specimen walls, the specimen end cross-sections are carefully inserted into the circular mold filled with PVC (poly-vinyl chloride) epoxy-resin, as shown in Fig. 7(b).

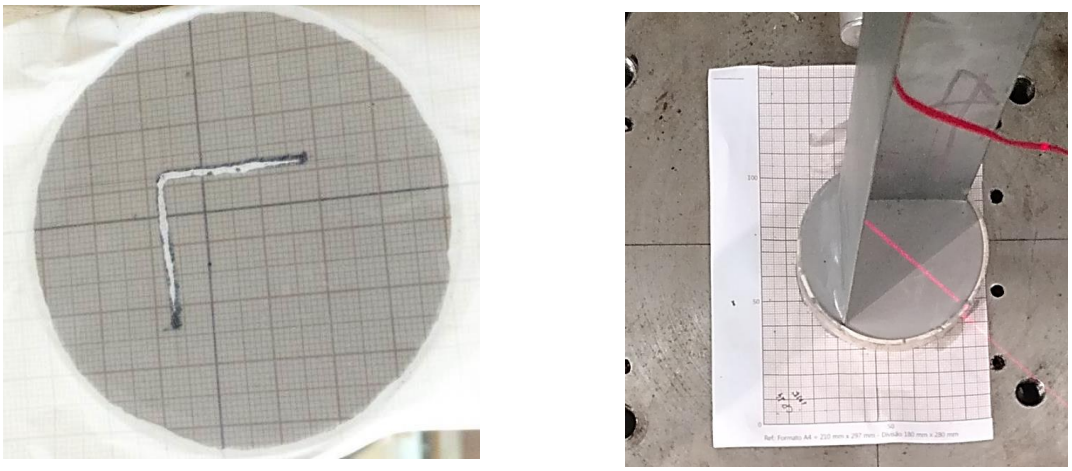

(a) (b)

Figure 7: (a) Positioning of the specimen on the "1 mm square grid graph paper" and (b) bottom view of the specimen top end cross-section are embedded into the epoxy-resin PVC epoxy-resin plate.

(iv) Then, the PVC (poly-vinyl chloride) epoxy-resin plates embedding the specimen end cross-sections are carefully positioned with respect to the top and bottom spherically-hinged supports (see Figs. 6(a)-(b)), making sure that their centroids are as aligned as possible. After connecting the above plates and supports the hydraulic jack actuator was moved slowly towards the specimen until the top support arrangement (previously put in place and adequately bolted to the hydraulic jack loading plate, with the various plate centroids as aligned as possible) until full contact was achieved. Then, after the appropriate horizontal positioning of the specimen is completed, the top spherically-hinged support bolts are tightened and the whole specimen positioning procedure is finished. In view of this careful procedure, it seems fair to argue that the tests are performed under virtually concentric loading conditions (the load eccentricity will certainly be extremely small and, therefore, can be neglected).

4.4 Displacement Measurements

Two sets of displacement measurements were made for each specimen, both of them by means of five displacement transducers (DTs) (i) able to move along the specimen outer surface prior to the test and (ii) placed at the specimen mid-height during the test. The DT arrangements (locations along the cross-section contour) involved in each set of displacement measurements are depicted in Figs. 8(a)-(b). The DT arrangements, carefully selected in order to enable capturing the column major-axis flexural-torsional and minor-axis flexural displacements, can be characterized as follows:

(i) The first arrangement concerns the measurement of the specimen initial geometrical imperfections (see Fig. 8(a)). Four DTs (DT1 to DT4) were supported by a (rigid) device mounted on a (also rigid) working table of a milling machine, which could move horizontally along the whole specimen length, guided and aligned by a transverse hand-wheel. The position was monitored by means of a fifth DT (DT5) – wire potentiometer-type displacement transducer.

(ii) The second arrangement involves four DTs (DT1 to DT4 –see Fig. 8(b_1)) providing measurements throughout the entire test duration, thus making it possible to assess the evolution of the specimen mid-height global displacements. An additional DT (DT5) was placed at the upper face of the top spherically hinged plate support device (see Fig. 8(b_2)), to measure the specimen axial shortenings.

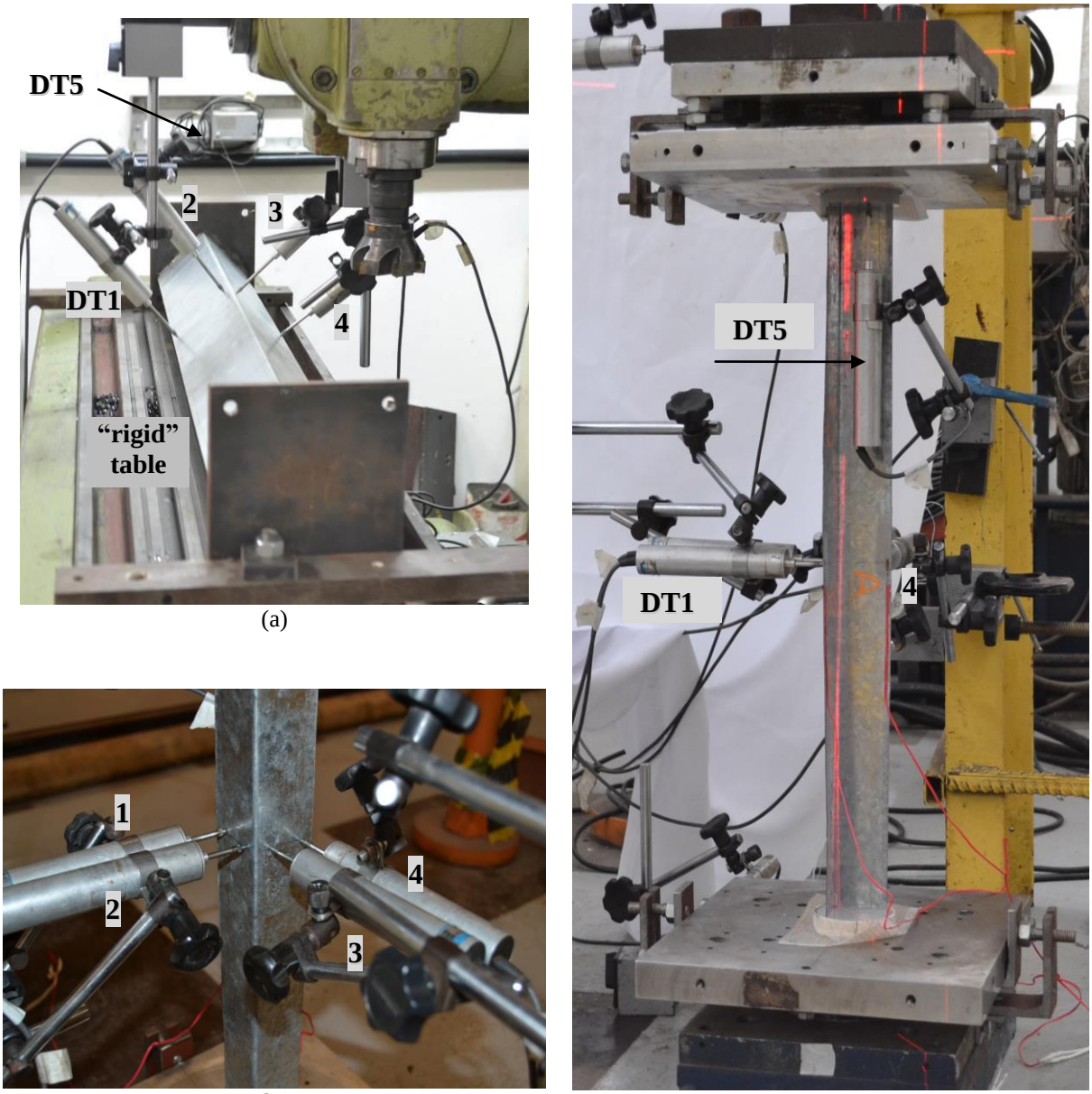

(a)

(b_1) (b_2)

Figure 8: DT arrangements to measure the specimens (a) initial geometrical imperfections (prior to the test) and (b) mid-height displacements (during the test) – (b_1) zoomed mid-height region and (b_2) overall view.

4.5 Test Procedure

Each column specimen test involved the sequential performance of the following tasks:

(i) Manufacture of the *15mm* thick epoxy resin plates by means of a PVC cast.

(ii) Positioning of the specimen on the spherical support using "*1 mm* square grid graph paper", thus ensuring negligible load eccentricity.

(iii) Place five DT transducers, four of which at the column mid-height and one at the center of the upper face of the top PVC epoxy-resin plate.

(iv) Slow (*0.005mm/s)* loading and unloading of an initial small compressive load (*1-2kN*), aimed at eliminating gaps between the spherically-hinged supports and the specimen end plates.

(v) Application of the displacement-controlled loading, by means of the UTM servo-controlled hydraulic actuator, at a sufficiently low rate to preclude relevant dynamic effects (*0.005mm/s*).

(vi) Continuous recording, by means of a *15Hz* data acquisition system, of the DT outputs and load cell readings.

(vii) Photograph the specimen deformed configurations during the test as the load approaches the predicted ultimate strength, to ensure that experimental evidence of column failure mode nature is obtained and well documented.

4.6 Test Results

The experimental results obtained from this test campaign consist of column (i) initial geometrical imperfection configurations, (ii) equilibrium paths, relating the applied load to relevant displacements, (iii) failure load data and (iv) deformed configurations (including the failure modes) evidencing the presence of flexural and torsional deformations. Since the *19* column specimens tested shared essentially the same structural response, only a representative sample of these various types of experimental results are individually reported and discussed in the following subsections – the whole set of experimental results has been reported by Santana (2018).

4.6.1 Initial geometrical imperfections

Initial geometrical imperfections were measured by spanning the transducers DT1 to DT4 (locations shown in Fig. 9(a)) along the specimen length. Table 3 provides (i) the maximum and minimum values recorded, along the specimen length, by each transducer (DT1-4) and (ii) the computed values of the torsional rotation (β) and translations due to major and minor-axis flexure (d_M and d_m, respectively). This computation procedure, which was previously described in detail by Landesmann *et al.* (2016), (i) is based on the fact that the cross-sections undergo rigid-body motions and (ii) takes into account that the transducers DT1-4 remain fixed while the measured cross-sections move (this also applies to the evaluation of the β, d_M and d_m values due to the applied load – see Section 4.6.2) and (iii) is summarized as follows (and also illustrated in Figs. 9(a)-(b)):

(i) Fig. 9(a) shows an undeformed cross-section, lying on the X-Y plane, and the locations of the four DTs: (i_1) DT1-2 are placed normally to the "vertical" leg at distances $y_1=(b-5)\,mm$ and $y_2=5\,mm$ from the corner, and (i_2) DT3-4 are placed normally to the "horizontal" leg, at distances $x_3=5\,mm$ and $x_4=(b-5)\,mm$ from the corner[5]. The signs of the displacements measured by the DTs are in accordance with the coordinate system *x-y* associated with the *X-Y* axes – moreover, the torsional rotation angles β are positive clockwise, as illustrated by the deformed configuration in Fig. 9(b).

(ii) The cross-section torsional rotation β is straightforwardly obtained from one of the expressions

$$\beta = \tan^{-1}\left(\frac{\mathrm{DT1}-\mathrm{DT2}}{y_2-y_1}\right) \quad \text{or} \quad \tan^{-1}\left(\frac{\mathrm{DT4}-\mathrm{DT3}}{x_4-x_3}\right) \ , \tag{12}$$

(iii) The measurements of the transducers DT1 and DT4 can be expressed, in terms of d_H, d_V and β, as (see Fig. 9(b))

$$\mathrm{DT1} = d_H - \left(y_1 - d_V\right)\tan\beta \tag{13}$$

$$\mathrm{DT4} = d_V + \left(x_4 - d_H\right)\tan\beta \ . \tag{14}$$

[5] In the C1 columns the DTs were placed as follows: $y_1=(b-3)\ mm$, $y_2=3\ mm$, $x_3=3\ mm$ and $x_4=(b-3)\ mm$.

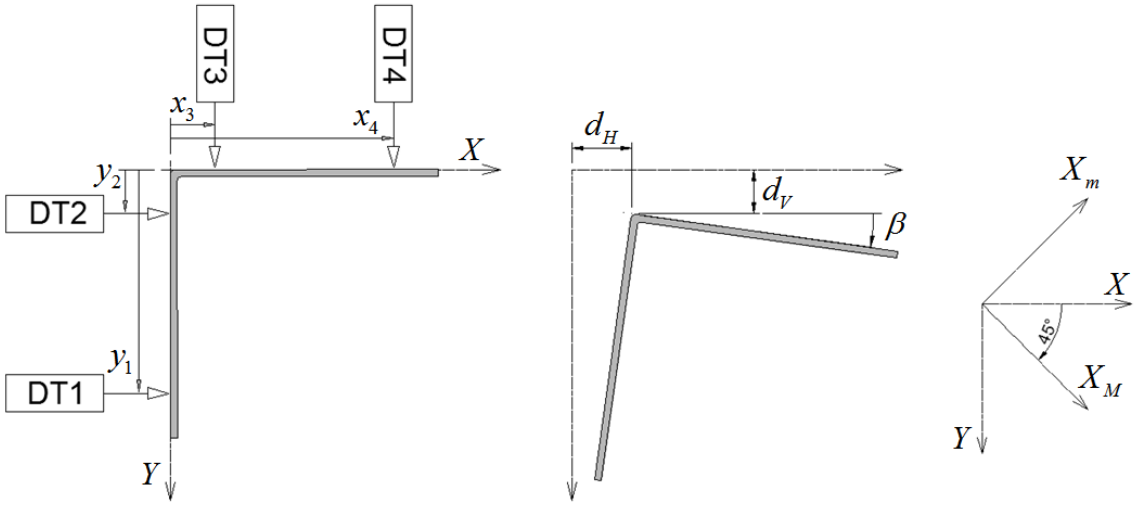

(a) (b) (c)

Figure 9: (a) Cross-section undeformed configuration and DT locations, (b) cross-section deformed configuration and definition of d_H, d_V and β, and (c) change of coordinate axes, required to determine d_M and d_m (Landesmann *et al.* 2016).

Table 3: Measured and calculated maximum/minimum specimen initial displacement and rotation values (*mm* and *rad x* 10^2)

Column	DT1	DT2	DT3	DT4	d_{m0}	d_{M0}	β_0
C1-400	0.886/0.0001	0.379/0.0001	0.113/-0.143	0.228/-0.429	0.274/-0.03	0.476/0.0001	0.0001/-2.082
C1-400R	0.963/-0.133	0.069/-0.239	0.173/-0.257	0.0001/-0.845	0.094/-0.353	0.249/-0.333	0.0001/-3.992
C1-600	1.297/0.0001	0.145/-0.012	0.286/-0.015	0.528/0.0001	0.025/-0.228	0.965/0.0001	0.088/-2.784
C1-800	0.256/-0.061	0.206/0.0001	0.0001/-0.85	0.268/0.0001	0.862/0.0001	0.378/-0.043	3.049/0.005
C2-400	0.947/-0.718	0.423/-0.845	0.231/-0.664	0.545/-0.520	0.619/-0.214	0.53/-0.852	0.397/-0.336
C2-400R	0.607/-1.427	0.303/-1.005	0.743/-1.003	1.233/-1.399	0.849/-1.128	0.168/-1.334	1.111/-0.945
C2-600	0.774/-0.805	0.178/-0.537	0.122/-0.395	0.0001/-0.789	0.0001/-0.134	0.052/-0.909	0.278/-1.814
C2-600R	0.158/-1.229	0.166/-0.513	0.464/-0.106	0.516/-0.128	0.179/-0.562	0.042/-0.549	1.102/-0.121
C2-800	0.591/-0.474	0.946/-0.159	0.631/-0.223	1.342/-0.491	0.729/-0.236	0.716/-0.135	1.616/0.0001
C3-400	0.998/0.0001	0.449/-0.015	0.046/-0.461	0.074/-0.759	0.557/-0.042	0.389/0.0001	0.0001/-1.071
C3-600	0.168/-1.273	0.0001/-0.779	0.717/-0.488	1.343/-0.888	0.151/-0.966	0.037/-0.546	1.432/-0.961
C3-600R	0.832/-0.322	0.081/-0.311	0.416/-0.352	0.209/-1.391	0.133/-0.561	0.0001/-0.44	0.086/-2.235
C3-800	0.624/-0.965	0.0001/-0.783	0.901/-0.054	0.982/-0.489	0.0001/-1.131	0.313/-0.499	0.553/-1.534
C3-1000	0.25/-1.303	0.042/-0.935	0.633/-0.21	1.352/-0.861	0.03/-1.012	0.055/-0.678	1.37/-1.219
C4-400	1.328/-0.444	0.634/-0.275	0.518/-0.174	0.673/-0.498	0.49/-0.436	0.606/-0.038	0.587/-1.265
C4-600	1.197/0.0001	0.555/-0.037	0.151/-0.258	0.0001/-0.816	0.422/0.0001	0.632/-0.042	0.12/-1.549
C4-600R	0.37/-0.274	0.643/-0.075	0.21/-0.092	0.022/-1.037	0.374/-0.061	0.0001/-0.656	0.351/-1.178
C4-800	1.297/-0.941	0.575/-0.514	0.207/-0.288	0.331/-0.883	0.483/-0.406	0.444/-0.664	0.617/-1.61
C4-1000	0.42/-0.62	0.174/-0.375	0.188/0.0001	1.132/-0.048	0.093/-0.347	0.68/-0.366	1.463/0.0001

(v) The last step consists of expressing the cross-section corner location through its coordinates along the centroidal principal axes (d_M and d_m), forming *45°* angles with the leg ("horizontal" and "vertical") directions – this straightforward procedure is illustrated in Fig. 9(b) and leads to

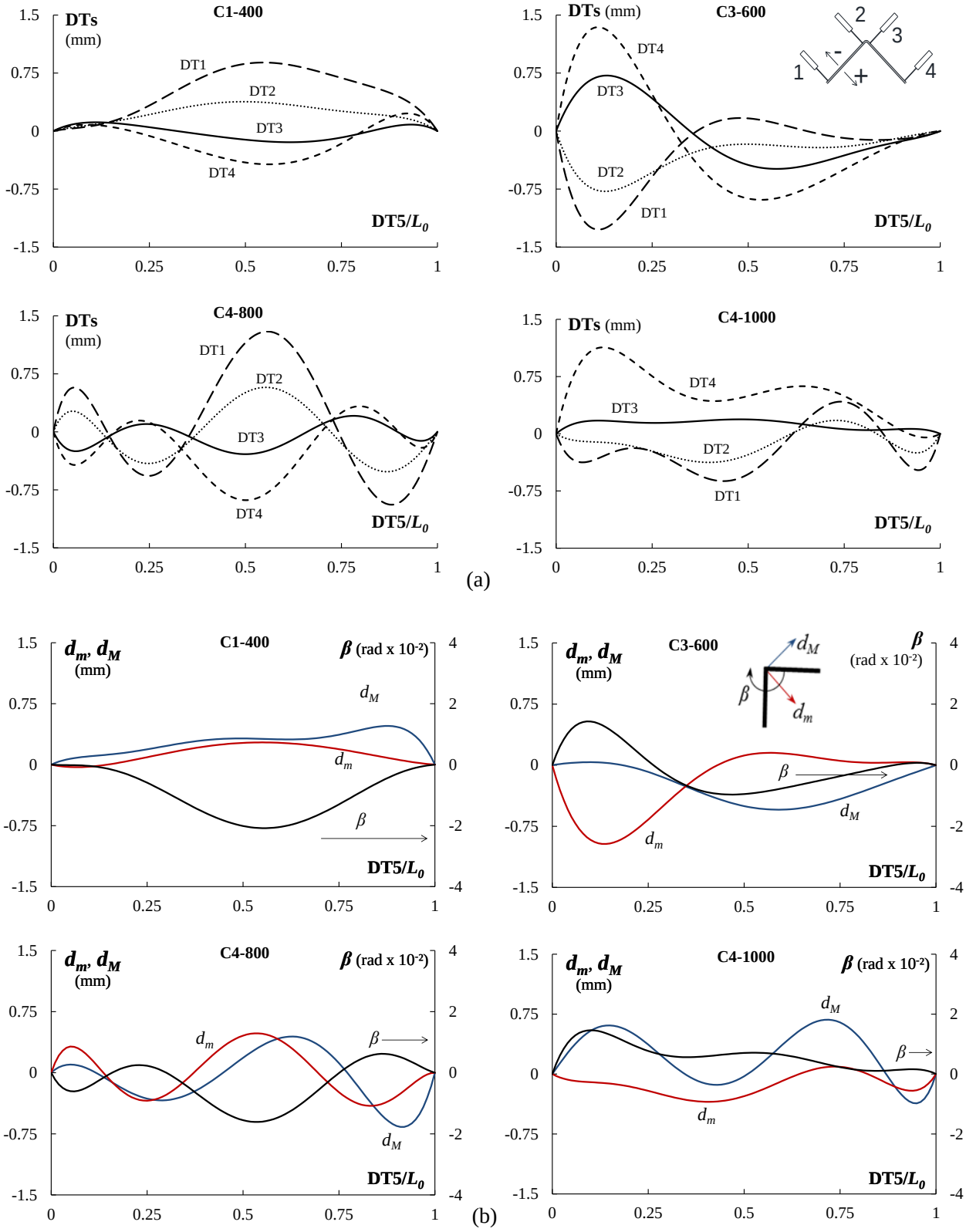

Figure 10: Initial displacement and rotation longitudinal profiles (horizontal coordinate normalized with respect to L_0) concerning specimens C1-400+C3-600+C4-800+C4-1000: (a) DT1-4 readings and (b) β, d_M and d_m values.

$$d_M = \left(d_H + d_V\right)\sqrt{2}/2 \tag{15}$$

$$d_m = \left(d_H - d_V\right)\sqrt{2}/2 \quad . \tag{16}$$

As for Figs. 10(a)-(b), they show the initial displacement/rotation longitudinal profiles acquired from the tests involving specimens C1-400, C3-600, C4-800 and C4-1000, which were obtained either (i) directly from the DT1-4 readings or (ii) using Eqs. (12)-(14) (β, d_M and d_m). Note that (i) the horizontal coordinates are normalized with respect to the column measured length L_0 (DT5/L_0) and (ii) the sign assumed for the transducer readings is also indicated (positive/negative readings for outward/inward displacements, respectively). The observation of these results prompts the following remarks:

(i) The DT1-4 measurements are fairly small, as their maximum absolute values range between *0.8 mm* and about *1.45 mm*, *i.e.*, very close to the nominal wall thicknesses.

(ii) All displacement profiles provided by the DT1-4 readings exhibit (ii_1) some degree of asymmetry and (ii_2) a dominant single half-wave sinusoidal shape, combined with minor participations from two and three half-wave sinusoids.

(iii) Logically, the maximum d_M and d_m values are also quite small: about *1.34 mm* and *1.13 mm*, respectively. Moreover, the d_M/L_0 and d_m/L_0 ratios (iii_1) vary from 5.47×10^{-6} to 3.33×10^{-3} and from 1.22×10^{-6} to 2.82×10^{-3}, respectively, and (iii_2) exceed *L/1000* in columns C1-400, C1-600, C2-400, C4-400 and, C4-600 (d_M), and C1-800, C2-400, C2-400R, C3-400 and, C4-400 (d_m). Finally, the mid-span torsional rotation β ranges between -3.992×10^{-2} and 3.049×10^{-2} *rad*.

4.6.2 Equilibrium paths

Figure 11 shows the equilibrium paths obtained from the tests of specimens C1-400, C3-600 and C4-800, relating the applied load *P*, provided by the hydraulic actuator load cell, to (i) the axial shortening Δ (DT5 reading) and (ii) the mid-height torsional rotation β and translations associated with minor-axis (d_m) and major-axis (d_M) flexure. The β, d_m and d_M values are those caused by the applied load (*i.e.*, do not include the initial values). The observation of such equilibrium paths prompts the following comments:

(i) The equilibrium paths *P vs.* Δ exhibit initial portions that are virtually linear, corresponding to column axial stiffness values equal to EA/L_0=*209.4-332-312.5 kN/cm* for the C1-400, C3-600, C4-800 columns, respectively. Note also that both (i_1) the applied load level associated with the transition to a non-linear curve and (i_2) the length of this non-linear curve portion, prior to failure, vary visibly – they increase with both (i_1) the column critical buckling load and (i_2) parameter Δ_f (see Table 1).

(ii) The equilibrium paths *P vs.* β and *P vs.* d_M must be viewed as a "unit", since they correspond to a single deformation pattern, akin to the flexural-torsional buckling mode. Indeed, they follow very similar trends (accounting for the scale differences, of course). However, because the flexural-torsional buckling mode is predominantly torsional, the torsional rotations clearly overshadow the major-axis flexural displacements.

(iii) The equilibrium paths *P vs.* d_m only branch out from the null displacement vertical axis at relatively advanced loading stages. This is due to the fact that such displacements, which rapidly become much larger than their d_M counterparts, stem from a combination of (iii_1) effective centroid shift effects, which occur in all columns, and (iii_2) interaction with minor-axis flexural buckling, which is most relevant in the columns exhibiting close flexural-torsional and flexural buckling loads. In the column specimens tested in this work, the latter aspect has little relevance, since f_{crft} and f_{cre} are almost always very far apart (see Table 5) – the only exception is column C1-800, for which f_{cre} is only *20%* above f_{crft} – this issue is further discussed in Section 4.6.3.

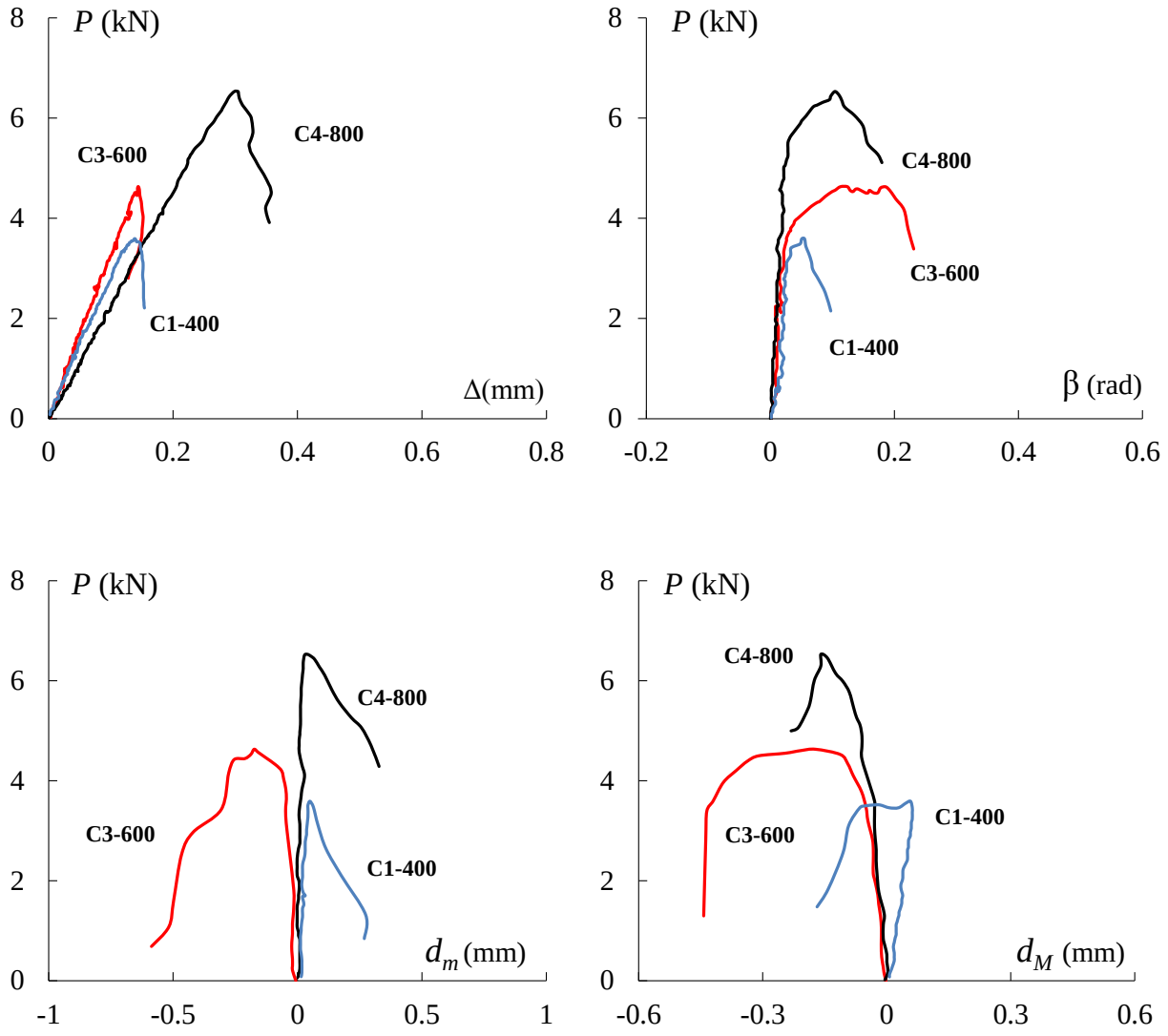

Figure 11: C1-400, C3-600 and C4-800 column experimental equilibrium P vs. Δ, P vs. β, P vs. d_m and P vs. d_M.

4.6.3 Failure loads

Table 4 provides the column experimental failure loads $P_{u.Exp}$, squash loads P_y, $P_{u.Exp}/P_y$ ratios and failure mode natures. The P_y values are based on (i) areas A obtained with the average values of the measured cross-section dimensions (neglecting the rounded corners – see Table 2) and (ii) a yield stress $f_y=366MPa$ (average of the values obtained from the tensile coupon tests presented in Section 4.2). The specimens failed in modes exhibiting either (i) highly predominant major-axis flexural-torsional deformations (termed "FT") or (ii) combining major-axis flexural-torsional deformations with visible minor-axis flexural ones (termed "FT+F"). The latter was found to occur only for specimen C1-800, which has the shortest leg width and the longest length (for the geometry set considered), as reflected in the fact that f_{cre} is only *20%* above f_{crft} (see Table 5)[6]. This is just a logical consequence of the occurrence of fairly strong interaction between the two buckling modes – see item (iii) in Section 4.6.2. Moreover, it should also

[6] The careful displacement measurements reveal that the specimens failing in FT modes also exhibit minor-axis flexure, which only appears very close to failure. Nevertheless, the d_m displacements are not visible by the naked eye, except those exhibited by the C1-800 specimen, which fails in a clear FT+F mode.

be noted that all specimens have $P_{u.Exp}/P_y$ below *0.24*, which is in accordance with their high slenderness values (plasticity plays a lesser role in the column failure). Finally, it is still worth noting that the failure loads of the repeated tested specimens (C1-400R, C2-400R, C2-600R, C3-600R, C4-600R) differ from their original counterparts by *–7.2%*, *–5.7%*, *–8.3%*, *–7.6%* and *+6.5%*, thus evidencing a fairly good test repeatability – note that the pairs of column specimens contain different initial geometrical imperfections.

Table 4: Experimental results: column failure loads, squash loads and observed failure mode natures.

Column	$P_{u.Exp}$ (kN)	P_y (kN)	$\frac{P_{u.Exp}}{P_y}$	Failure mode
C1-400	3.59	15.01	0.24	FT
C1-400R	3.33	14.93	0.22	FT
C1-600	3.4	15.43	0.22	FT
C1-800	2.81	14.97	0.19	FT+F
C2-400	3.87	29.29	0.13	FT
C2-400R	3.65	28.75	0.13	FT
C2-600	3.15	29.85	0.11	FT
C2-600R	2.89	30.45	0.09	FT
C2-800	3.2	29.40	0.11	FT
C3-400	5.9	35.04	0.17	FT
C3-600	4.63	35.59	0.13	FT
C3-600R	4.28	35.59	0.12	FT
C3-800	3.65	35.04	0.10	FT
C3-1000	3.72	35.03	0.11	FT
C4-400	9.3	45.11	0.21	FT
C4-600	5.96	45.52	0.13	FT
C4-600R	6.35	45.66	0.14	FT
C4-800	6.53	44.52	0.15	FT
C4-1000	5.94	45.03	0.13	FT

4.6.4 Deformed configurations and failure modes

Figs. 12(a)-(b) concern specimen C3-600 and provide its (i) equilibrium path *P vs. Δ* and (ii) deformed configuration evolution during the test (*i.e.*, as the applied load grows) – the six deformed configurations shown in Fig. 12(b) correspond to the equilibrium states *I* to *VI* indicated by yellow circles on the equilibrium path depicted in Fig. 12(a). On the other hand, Figs. 13(a)-(c) and 14(a)-(b) show (i) the deformed configurations, at the onset of collapse ($P \approx P_{u.Exp}$), of specimens C1-400, C1-600 and C1-800, (ii) a close view of the specimen C1-400 most deformed region immediately after collapse and (iii) a joint view of the deformed shapes of the four C1 specimens after the load removal. The observation of these column deformed configurations makes it possible to conclude that:

(i) The evolution of the specimen C3-600 deformed configuration, depicted in Fig. 12(b), clearly illustrates the emergence and development of predominantly torsional flexural-torsional deformations towards failure in a single half-wave FT mode, akin to the column critical buckling mode[7].

[7] Of course, the designation "single half-wave" takes into account the two "quarter-waves" appearing near the specimen supports, fixed with respect to torsion and major-axis flexure. There are also minute (not visible by the naked eye, but revealed by the measurements) minor-axis flexural deformations due to the effective centroid shift effects (Dinis *et al.* 2012).

The specimen remains almost undeformed until state *I* (about *30%* of the failure load). However, beyond this stage flexural-torsional displacements become clearly visible and grow progressively up to failure, which occurs at state *V*. After the peak load has been reached, the deformation becomes more pronounced, as illustrated by means of state *VI*.

(ii) The collapse mechanisms exhibited by all specimens are triggered by the formation of "plastic hinges" at the one and three quarter-height cross-sections, as can be observed in state *V* of Fig. 12(b) and in Figs. 13(a)-(c) – numerical evidence of this feature was recently reported by Landesmann *et al.* (2016), in the context of columns with cylindrically-hinged supports.

(iii) In order to assess the amount of elastic deformation undergone by the compressed columns during the test, which is subsequently recovered after the load removal, it suffices to compare the deformed configurations displayed in Figs. 13(a)-(c) and 14(a) with their counterparts in Fig. 14(b) – they all concern C1 columns.

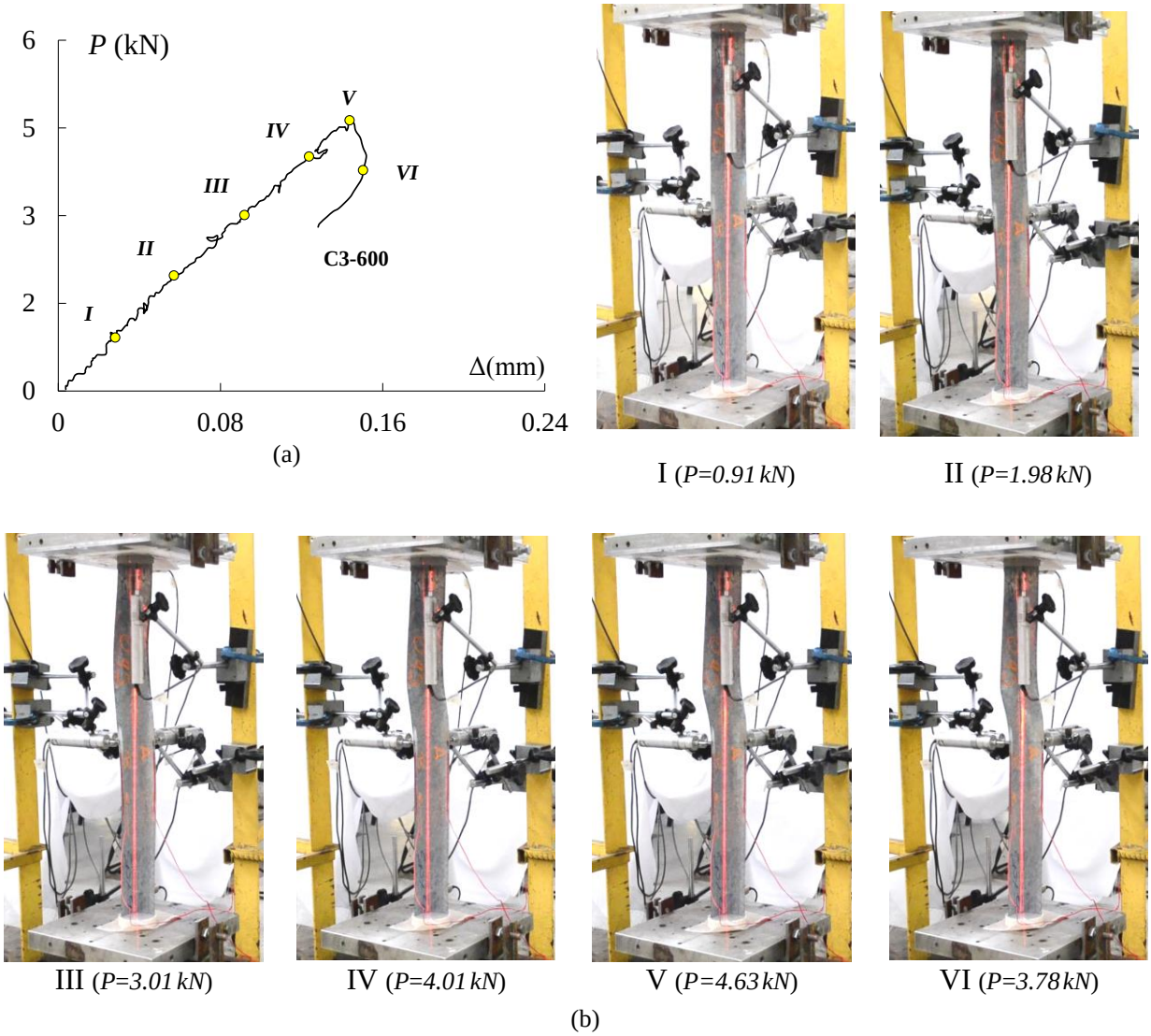

Figure 12: C3-600 specimen (a) equilibrium path *P* vs. Δ and (b) deformed configuration evolution.

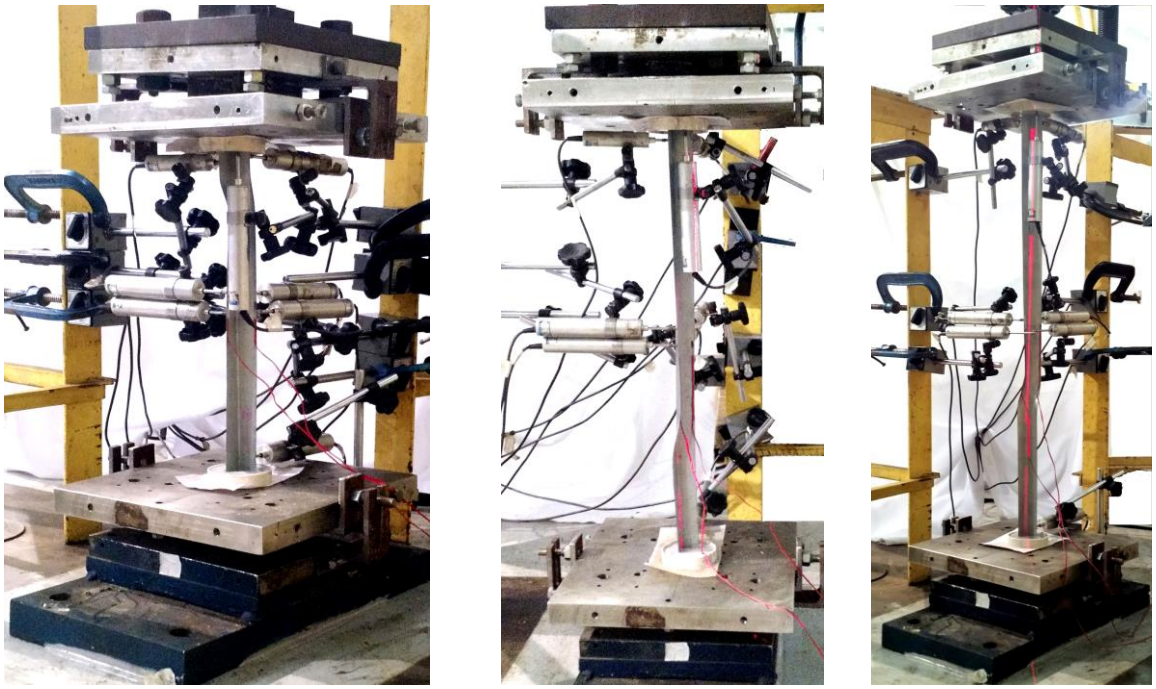

(a) (b) (c)

Figure 13: Deformed configurations at the onset of collapse of specimens (a) C1-400, (b) C1-600 and (c) C1-800.

(a) (b)

Figure 14: (a) Close view of the most deformed region of specimen C1-400 immediately after collapse and (b) joint view of the C1 column specimens after the load removal.

5. Assessment of the Proposed DSM Design Approach

Attention is now turned to assessing the performance of the DSM-based design approach proposed by Dinis & Camotim (2017), which was briefly presented in Section 2. The ultimate strength predictions provided by this approach (f_{nfte}) for the columns that were tested in this work are given in Table 5, together with the corresponding failure-to-predicted ultimate strength ratios f_u/f_{nfte}. On the other hand, Figure 15 plots, against λ_{fte}, the (i) experimental f_u/f_{nfte} values obtained in this work (grey circles)

and (ii) the numerical ones reported by Dinis & Camotim (2017) (white circles). The latter concern *144* short-to-intermediate columns with lengths and yield stresses (elastic-perfectly plastic material model) selected to ensure covering a wide slenderness range ($0.87 \leq \lambda_{fte} \leq 3.49$). Moreover, all the SH columns analyzed contained initial geometrical imperfections combining (i) a critical flexural-torsional component, with amplitude equal to 10% of the wall thickness *t*, and (ii) a non-critical minor-axis flexural component, with amplitude equal to *L*/1000 (leg tips under compression – most detrimental situation), values that are in line with the measured ones reported by Popovic *et al*. (1999). Finally, note that the residual stress and corner enhancement effects were disregarded in the parametric study of Dinis & Camotim (2017).

Moreover, the statistical indicators (averages, standard deviations and maximum/minimum values) concerning (i) the experimental failure loads, obtained in this work, (ii) the numerical failure loads, reported by Dinis & Camotim (2017), and (iii) both of them are provided in Table 6. The observation of the results presented in Fig. 15 and Tables 5 and 6 prompts the following remarks:

(i) The experimental failure loads obtained in this work are quite efficiently predicted by the DSM-based design approach proposed by Dinis & Camotim (2017), even if a fair underestimation is observed. Indeed, the f_u/f_{nfte} average, standard deviations and maximum/minimum values read *1.36-0.20-1.71-0.98* – note, in particular, the rather high standard deviation. These indicators are clearly more conservative and scattered than their numerical failure load counterparts, which read *1.06-0.08-1.26-0.91*. If both the experimental and numerical failure loads are considered together, the above indicators become*1.09-0.14-1.71-0.91*.

Table 5: SH column buckling and ultimate stresses, DSM estimates and experimental-to-predicted ratios (stresses in MPa)

Column	f_{bf}	f_{crft}	f_{cre}	f_u	Δ_f	a	b	c	d	β	λ_{fte}	f_{nfte}	$\frac{f_u}{f_{nfte}}$
C1-400	1376	77.8	343.9	88.27	2.20	0.46	0.14	0.36	0.87	0.52	1.74	67.6	1.31
C1-400R	1367	78.5	341.8	81.78	2.23	0.46	0.15	0.36	0.87	0.52	1.73	69.24	1.22
C1-600	633	73.9	158.1	82.28	4.73	0.58	0.16	0.29	0.92	0.64	1.37	54.39	1.48
C1-800	344	71.0	86.1	69.39	8.88	0.80	0.18	0.12	0.99	0.74	1.03	45.73	1.55
C2-400	5247	22.8	1311.7	47.74	0.16	0.40	0.15	0.54	0.66	0.31	3.78	33.81	1.45
C2-400R	5066	23.6	1266.6	46.85	0.18	0.40	0.15	0.52	0.69	0.30	3.71	33	1.41
C2-600	2434	20.5	608.6	38.48	0.32	0.40	0.15	0.43	0.81	0.26	3.72	24.59	1.58
C2-600R	2533	19.8	633.3	34.83	0.29	0.40	0.15	0.43	0.81	0.25	3.81	24.04	1.46
C2-800	1328	20.6	332.1	40.1	0.59	0.40	0.14	0.42	0.82	0.28	3.35	23.54	1.71
C3-400	5239	33.0	1309.9	62.23	0.24	0.40	0.15	0.44	0.81	0.30	3.14	37.48	1.65
C3-600	2411	29.9	602.8	48.07	0.47	0.40	0.14	0.43	0.82	0.31	3.08	33.4	1.43
C3-600R	2403	29.9	600.8	40.04	0.47	0.40	0.14	0.43	0.82	0.31	3.08	33.17	1.20
C3-800	1307	29.9	326.8	38.5	0.87	0.40	0.14	0.41	0.83	0.33	2.77	31.67	1.21
C3-1000	836	29.5	209.1	39.28	1.35	0.42	0.14	0.39	0.84	0.37	2.44	28.85	1.35
C4-400	5290	53.7	1322.5	75.85	0.38	0.40	0.15	0.43	0.82	0.38	2.46	57.26	1.34
C4-600	2433	47.6	608.4	48.27	0.74	0.40	0.14	0.41	0.83	0.38	2.44	49.42	0.98
C4-600R	2449	47.3	612.2	61.12	0.73	0.40	0.14	0.41	0.83	0.38	2.45	49.09	1.24
C4-800	1308	48.1	327.1	54.07	1.41	0.42	0.14	0.39	0.84	0.41	2.18	45.49	1.18
C4-1000	841	47.6	210.3	48.89	2.20	0.46	0.15	0.36	0.87	0.46	1.93	41.4	1.17

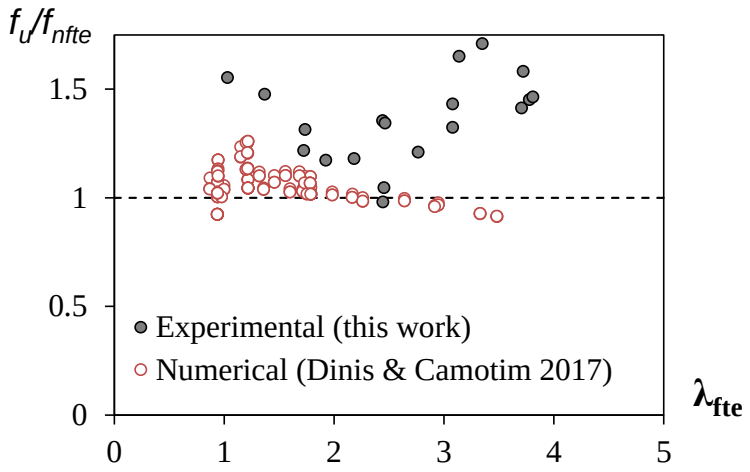

Figure 15: f_u/f_{nfte} vs. λ_{fte} plots concerning the (i) experimental failure loads obtained in this work and (ii) the numerical failure loads reported by Dinis & Camotim (2017).

Table 6: Averages, standard deviations and maximum/minimum values of f_u/f_{nfte} concerning the experimental failure loads obtained in this work, the numerical failure loads reported by Dinis & Camotim (2017) and both of them.

f_u / f_{nfte}	Mean	Sd. Dev.	Max	Min
Experimental (this work)	1.36	0.20	1.71	0.98
Numerical (Dinis & Camotim 2017)	1.06	0.08	1.26	0.91
Experimental + Numerical	1.09	0.14	1.71	0.91

(ii) The underestimation of the experimental failure loads mostly stems from the differences between the initial geometrical imperfection minor-axis flexural components exhibited by the column specimens tested in this work and those adopted to obtain the numerical failure loads employed to develop and calibrate the DSM-based design approach (Dinis & Camotim 2017) – recall that the latter have an amplitude equal to $L/1000$ and, above all, are associated with leg tips under compression, which corresponds to the most detrimental situation. Since the vast majority of the column specimens tested contained initial minor-axis flexural displacements associated with the leg tips under tension, which "improve" the column strength (they "oppose" the effective centroid shift effects) – this can be attested by looking at Table 3 and noticing the majority of positive d_{m0} values measured.

(iii) In view of the content of the previous item, it is just logical to expect that a fair portion of the experimental failure loads obtained are underestimated by the DSM-based design approach. This is a direct consequence of (iii$_1$) the significant sensitivity of the equal-leg angle column failure loads to the "sign" (mostly) and amplitude of the minor-axis flexural initial imperfections and (iii$_2$) the fact that the design approach under consideration was developed assuming the most detrimental minor-axis flexural initial imperfections. A similar situation was recently reported by Landesmann *et al.* (2016), in the context of cylindrically-hinged short-to-intermediate equal-leg angle columns.

(iv) It is fair to argue that the test results reported in this work provide adequate experimental validation for the DSM-based design approach proposed by Dinis & Camotim (2017), thus paving the way for its codification in the not too distant future.

5.1 Load and Resistance Factor Design (LRFD)

This section addresses the evaluation of the LRFD (Load and Resistance Factor Design) resistance factor ϕ associated with the proposed DSM-based design approach. The North American specification for the design of cold-formed steel members (AISI 2016) stipulates that ϕ must be calculated by means of the formula (given in section F.1.1 of chapter F)

$$\phi = C_{\phi}(M_m F_m P_m)\, e^{-\beta_0 \sqrt{V_M^2 + V_F^2 + C_P V_P^2 + V_Q^2}} \qquad \text{with} \qquad C_P = \left(1 + \frac{1}{n}\right)\frac{m}{m-2} \quad , \qquad (17)$$

where (i) C_ϕ is a calibration coefficient (C_ϕ*=1.52* for LRFD), (ii) M_m*=1.10* and F_m*=1.00* are the mean values of the material and fabrication factors, respectively, (iii) β_0 is the target reliability index (β_0*=2.5* for structural members in LRFD), (iv) V_M*=0.10*, V_F*=0.05* and V_Q*=0.21* are the coefficients of variation of the material factor, fabrication factor and load effect, respectively[8], and (v) C_P is a correction factor that depends on the numbers of tests (n) and degrees of freedom (m=n-*1*). In order to evaluate ϕ for the proposed DSM procedure, it is necessary to provide P_m and V_P, the average and standard deviation of the f_u/f_{nfte} ratios – the f_u values are either experimental, numerical or both experimental and numerical.

Table 7 shows the n, C_P, P_m, V_P and ϕ values obtained for the column failure load predictions provided by the DSM-based design approach for the (i) experimental failure loads, (ii) numerical failure loads and (iii) both of them (whole set). It can be observed that:

(i) The sole consideration of the experimental failure loads obtained in this work leads to a resistance factor equal to ϕ*=1.02*, which is much higher than the value recommended in AISI (2016) for compression members (ϕ_c*=0.85*) and also visibly higher than the value obtained by considering only the numerical failure loads reported by Dinis & Camotim (2017) – ϕ*=0.94*. The resistance factor becomes equal to ϕ*=0.92* when both the experimental and numerical failure loads are considered.

(ii) The results obtained in this work provide experimental evidence that reinforces the conclusion drawn by Dinis & Camotim (2017): ϕ*=0.85* can be recommended for cold-formed steel angle columns designed with the proposed DSM-based approach. It is worth noting that the current North American specification for the design of cold-formed steel members (AISI 2016) allows for the DSM design of angle columns. However, the only possible option (with the codified strength curves) is to design the columns against local-global failures, which is conceptually wrong – moreover, Dinis & Camotim (2018) have very recently shown, in the context of fixed-ended and cylindrically-hinged short-to-intermediate equal-leg angle columns, that such an option leads to a resistance factor well below the value recommended in AISI (2016).

(iii) Finally, it seems fair to argue and conclude that the DSM-base design approach developed by Dinis & Camotim (2017) is ready for codification, thus supplementing similar design approaches already

Table 7: LRFD ϕ values obtained with the experimental failure loads, numerical failure loads and both of them.

Failure Loads	n	C_P	P_m	V_P	ϕ
Experimental (this work)	19	1.18	1.36	0.20	1.02
Numerical (Dinis & Camotim 2017)	144	1.02	1.06	0.08	0.94
Experimental + Numerical	163	1.02	1.09	0.14	0.92

[8] Values prescribed for concentrically loaded compression members – Chapter F, Section F1.1, Table F1 and text (AISI 2016).

proposed by these authors for fixed-ended and cylindrically-hinged short-to-intermediate equal-leg angle columns (Dinis & Camotim 2018). Such codification would enable an adequate design of such columns by means of the Direct Strength Method (this is not possible nowadays).

6. Concluding Remarks

The main aim of this work was to report the results of an experimental investigation, carried out at COPPE (Federal University of Rio de Janeiro), on the behavior and collapse of cold-formed steel spherically-hinged short-to-intermediate equal-leg angle columns (*i.e.*, buckling in flexural-torsional modes). This experimental study was performed to fill a gap in the available literature, recently detected and pointed out by Dinis & Camotim (2017), in the context of the development and performance assessment of a DSM-based design approach for such members. After presenting a brief overview of this design approach, the paper addressed the geometry selection of the column specimens, which involved sequences of linear buckling analyses and aimed at identifying column geometries covering a wide slenderness range. Next, detailed descriptions of the experimental test set-up and procedure were provided, including information on the fabrication and assembly of the spherically-hinged supports, on the careful specimen positioning, in order to minimize the load eccentricities, and on the displacement measurements (before and during the tests). Then, the experimental results obtained were presented and discussed – they included (i) initial geometrical imperfections, (ii) equilibrium paths relating the applied load to column displacements, (iii) failure loads and (iv) deformed configurations (including the collapse mechanisms).

In the last part of the paper, the *19* experimental failure loads obtained in this work and the *144* numerical failure loads reported by Dinis & Camotim (2017) were used to assess the performance of the DSM-based design approach proposed by these authors, who specifically developed and validated it in the context of spherically-hinged short-to-intermediate equal-leg angle columns. It was shown that both the experimental and numerical failure loads are both efficiently (safely and fairly accurately) predicted by the design approach, even if the former are visibly more underestimated. This stems from the significant sensitivity of the equal-leg angle column failure loads to the "sign" of the minor-axis flexural initial imperfections – impossible to "control" in the tested specimens and deemed the most detrimental in the numerical simulations. It seems fair to argue that this work provided adequate experimental validation for the previously proposed DSM-based design approach. In particular, note that it was concluded that the LRFD resistance factor currently prescribed in AISI (2016) for compression members ($\phi_c=0.85$) can also be reliably adopted for spherically-hinged short-to-intermediate equal-leg angle columns – recall that the same conclusion has already been reached for their fixed-ended and cylindrically-hinged counterparts (Dinis & Camotim 2018), but with a different set of flexural-torsional strength curves. This justifies the belief that it will be possible to achieve the joint codification of a DSM-based design approach for fixed-ended, cylindrically-hinged and spherically-hinged short-to-intermediate equal-leg angle columns in the not too distant future. The only question that will remain open is how does the above design approach handle columns with supports that partially restrain the flexural rotations – the authors are currently working towards finding answers for this question.

Acknowledgments

The first and second authors gratefully acknowledge the financial support of the Brazilian institutions CAPES (*Coordenação de Aperfeiçoamento de Pessoal de Nível Superior* – Finance Code 001), CNPq (*Conselho Nacional de Desenvolvimento Científico e Tecnológico*) and FAPERJ (*Fundação Carlos Chagas Filho de Amparo à Pesquisa do Estado do Rio de Janeiro*).

References

AISI (American Iron and Steel Institute) (2016). *North American Specification (NAS) for the Design of Cold-Formed Steel Structural Members* (AISI-S100-16) + respective *Commentary*, Washington DC.

ASTM (American Society for Testing and Materials) (2011). *Standard Specification for Steel Sheet, Zinc-Coated (Galvanized) or Zinc-Iron Alloy-Coated (Galvannealed) by the Hot-Dip Process*, ASTM A653, West Conshohocken.

ASTM (American Society for Testing and Materials) (2015). *Test Methods for Tension Testing of Metallic Materials*, ASTM E8/E8M-15a, West Conshohocken.

Bebiano R, Camotim D, Gonçalves R (2018). GBTUL 2.0 – A second-generation code for the GBT-based buckling and vibration analysis of thin-walled members, *Thin-Walled Structures*, **124**(March), 235-253.

Camotim D, Dinis PB, Martins AD (2016). Direct Strength Method (DSM) – a general approach for the design of cold-formed steel structures, *Recent Trends in Cold-Formed Steel Construction*, C. Yu (ed.), Woodhead Publishing (Series in Civil and Structural Engineering), Amsterdam, 69-105.

Chodraui GMB, Shifferaw Y, Malite M, Schafer BW (2006). Cold-formed steel angles under axial compression, *Proceedings of 18th International Specialty Conference on Cold-Formed Steel Structures* (Orlando, 26-27/10), R. LaBoube, W.W. Yu (eds.), 285-300.

Dinis PB, Camotim D (2015). A novel DSM-based approach for the rational design of fixed-ended and pin-ended short-to-intermediate thin-walled angle columns, *Thin-Walled Structures*, **87**(February), 158-182.

Dinis PB, Camotim D (2016). Behavior and design of hot-rolled steel pin-ended short-to-intermediate angle columns, *USB Key Drive Proceedings of Seventh International Conference on Coupled Instabilities in Metal Structures* (CIMS 2016 – Baltimore, 7-8/11), Paper 23.

Dinis PB, Camotim D (2017). Spherically-hinged short-to-intermediate angle columns: stability, non-linear behavior and DSM design, *Website Proceedings of Structural Stability Research Council (SSRC) Annual Stability Conference* (San Antonio, 21-24/3).

Dinis PB, Camotim D (2018). Proposal to improve the DSM design of cold-formed steel angle columns: need, background, quality assessment and illustration, *Journal of Structural Engineering* (ASCE), accepted for publication.

Dinis PB, Camotim D, Preto V (2016). Behaviour and design of short-to-intermediate hot-rolled steel angle columns, *Proceedings of the International Colloquim on Stability and Ductility of Steel Stuctures* (SDSS 2016 – Timisoara, 30/5 to 1/6), D. Dubina, V. Ungureanu (eds.), Wiley/Ernst & Sohn (Mem Martins), 477-484.

Dinis PB, Camotim D, Silvestre N (2010). On the local and global buckling behaviour of angle, T-section and cruciform thin-walled columns and beams, *Thin-Walled Structures*, **48**(10-11), 786-797.

Dinis PB, Camotim D, Silvestre N (2012). On the mechanics of angle column instability, *Thin-Walled Structures*, **52**(March), 80-89.

Ellobody E, Young B (2005). Behavior of cold-formed steel plain angle columns, *Journal of Structural Engineering* (ASCE), **131**(3), 469-478.

Kitipornchai S, Albermani FGA, Chan SL (1990). Elastoplastic finite-element models for angle steel frames, *Journal of Structural Engineering* (ASCE), **116**(10), 2567-2581.

Kitipornchai S, Chan SL (1987). Nonlinear finite-element analysis of angle and tee beam-columns, *Journal of Structural Engineering* (ASCE), **113**(4), 721-739.

Landesmann A., Camotim D., Dinis P.B., Cruz R. (2016). Short-to-intermediate slender pin-ended cold-formed steel equal-leg angle columns: experimental investigation, numerical simulations and DSM Design, *Engineering Structures*, **132**(February), 471-493.

Maia WF, Neto JM, Malite M (2008). Stability of cold-formed steel simple and lipped angles under compression, *Proceedings of 19th International Specialty Conference on Recent Research and Developments in Cold-Formed Steel Design and Construction* (St. Louis, 14-15/10), R. LaBoube, W.-W. Yu (eds.), 111-125.

Mesacasa Jr. EC (2012). *Structural Behavior and Design of Cold-Formed Steel Angle Columns*, M.A.Sc. Thesis in Structural Engineering, School of Engineering of São Carlos, University of São Paulo, Brazil. (Portuguese)

Mesacasa Jr. EC, Dinis PB, Camotim D, Malite M (2014). Mode-interaction in thin-walled equal-leg angle columns, *Thin-Walled Structures*, **81**(August), 138-149.

Popovic D, Hancock GJ, Rasmussen KJR (1999). Axial compression tests of cold-formed angles, *Journal of Structural Engineering* (ASCE), **125**(5), 515-523.

Rasmussen KJR (2005). Design of angle columns with locally unstable legs, *Journal of Structural Engineering* (ASCE), **131**(10), 1553-1560.

Rasmussen KJR (2006). Design of slender angle section beam-columns by the direct strength method, *Journal of Structural Engineering* (ASCE), **132**(2), 204-211.

Santana KG (2018). *Direct Strength Method Design of Spherically-Hinged Cold-Formed Steel Equal-Leg Angle Columns*, M.A.Sc. Thesis in Structural Engineering, COPPE, Federal University of Rio de Janeiro, Brazil. (Portuguese)

Schafer B.W. (2008). Review: the direct strength method of cold-formed steel member design, *Journal of Constructional Steel Research*, **64**(7-8), 766-778.

Shifferaw Y, Schafer BW (2014). Cold-formed steel lipped and plain angle columns with fixed ends, *Thin-Walled Structures*, **80**(July), 142-152.

Young B (2004). Tests and design of fixed-ended cold-formed steel plain angle columns, *Journal of Structural Engineering* (ASCE), **130**(12), 1931-1940.